Zheng *et al. PhotoniX* (2025) 6:55
https://doi.org/10.1186/s43074-025-00214-2

PhotoniX

RESEARCH **Open Access**

V-pit-induced electric field redistribution enabling efficient hole injection in InGaN-based red light-emitting diodes grown on silicon

Xi Zheng[1,2], Guobao Zhao[1], Yurong Dai[1], Yi Fu[3], Mingbing Zhou[3], Tao Huang[3], Swee Tiam Tan[4], Vijay Kumar Sharma[2], Yijun Lu[1], Tingzhu Wu[1], Hilmi Volkan Demir[2,5], Zhong Chen[1*] and Weijie Guo[1*]

*Correspondence:
chenz@xmu.edu.cn;
wjguo@xmu.edu.cn

[1] National Innovation Platform for the Fusion of Industry and Education in Integrated Circuits, Department of Electronic Science, School of Electronic Science and Engineering, Xiamen University, Xiamen 361005, China
[2] LUMINOUS! Centre of Excellence for Semiconductor Lighting and Displays, School of Electrical and Electronic Engineering, School of Physical and Mathematical Science, School of Materials Science and Engineering, Nanyang Technological University, Singapore 639798, Singapore
[3] Latticepower Co. Ltd., Nanchang 330096, China
[4] Kelip-Kelip! Center of Excellence for Light Enabling Technologies, School of Energy and Chemical Engineering, Xiamen University Malaysia, Sepang, Selangor 43900, Malaysia
[5] Department of Electrical and Electronics Engineering, Department of Physics, Bilkent University UNAM-Institute of Materials Science and Nanotechnology and The National Nanotechnology Research Center, Bilkent University, Bilkent, Ankara 06800, Turkey

Abstract

InGaN-based micro-light-emitting diodes (micro-LEDs) have been widely recognized as one of the critical technologies for high-resolution display applications. However, achieving high-efficiency, environmental-friendly, and small-size self-emitting InGaN-based red micro-LEDs present significant challenges that impede the progress of monolithically integrated III-nitride full-color micro-LED displays. Current limitations stem from insufficient control over carrier dynamics in InGaN multiple quantum wells (MQWs), where conventional structures exhibit severe efficiency degradation due to insufficient hole injection and defect-induced nonradiative recombination. Herein, spatially-resolved in-situ hyperspectral imaging and numerical simulations demonstrate that optimized V-pit promote the effectiveness of three-dimensional current pathways and facilitate localized electric field redistribution. This improvement enhances hole injection while suppressing nonradiative recombination, this work contributes to the microstructure design in InGaN-based red LEDs.

Keywords: GaN-based LED, V-pit microstructure, Dislocation density, Microscopic hyperspectral imaging, Micro-LEDs

Introduction

Micro-light-emitting diodes (micro-LEDs) have garnered significant attention as one of the leading technologies for high-resolution display applications, including near-eye displays, wearable displays, and transparent displays [1–4]. Additionally, micro-LEDs are continuously revolutionizing various fields such as light communications, high-speed optical interconnects, sensing, among others. Among these advancements, InGaN-based blue and green micro-LEDs have demonstrated efficient emission; however, commercially available AlGaInP-based red micro-LEDs inevitably experience wavelength shift with temperature variations and are susceptible to efficiency degradation especially when operating under high current density due to Auger nonradiative recombination [5]. Moreover, AlGaInP-based micro-LEDs suffer from more severe sidewall effect when the dimensions are reduced to a few microns because of the long carrier diffusion length and high surface recombination velocity of this material [6, 7], which could adversely

© The Author(s) 2025. **Open Access** This article is licensed under a Creative Commons Attribution 4.0 International License, which permits use, sharing, adaptation, distribution and reproduction in any medium or format, as long as you give appropriate credit to the original author(s) and the source, provide a link to the Creative Commons licence, and indicate if changes were made. The images or other third party material in this article are included in the article's Creative Commons licence, unless indicated otherwise in a credit line to the material. If material is not included in the article's Creative Commons licence and your intended use is not permitted by statutory regulation or exceeds the permitted use, you will need to obtain permission directly from the copyright holder. To view a copy of this licence, visit http://creativecommons.org/licenses/by/4.0/.

affect the overall performance of full-color microdisplays. Moreover, the integration of phosphide micro-LEDs with InGaN-based green and blue devices introduces complexities in backplane fabrication and driving configurations.

Alternatively, InGaN-based red micro-LEDs have emerged as a promising candidate by incorporating high In-content InGaN into the active region [8, 9], which can potentially overcome these drawbacks, especially when used in augmented/virtual reality (AR/VR) applications [10–13]. However, these InGaN-based devices are still challenged by low external quantum efficiency (EQE), large full-width at the half maximum (FWHM), and wavelength shift [14, 15]. Although there have been previous reports on InGaN-based red micro-LEDs [16–20], achieving highly efficient devices has remained a pending challenge; this is particularly relevant to the hexagonal V-shaped pits induced by dislocations, which are typically formed during the lower-temperature epitaxial growth of high-In-content multiple quantum wells (MQWs) [21]. On the other hand, GaN-on-silicon substrates offer advantages in thermal expansion coefficient matching and ease of integration with complementary metal–oxide–semiconductor (CMOS) backplanes [22–24]. However, a comprehensive understanding of carrier dynamics, particularly within regions associated with V-pit microstructures on silicon substrates, remains incomplete.

In this work, we investigate the three-dimensional carrier transport mechanisms related to V-pits in the InGaN-based red LEDs, efficient emission from red MQWs can be achieved by reasonably modulating the V-pit density, which significantly enhances local hole injection efficiency. The in-situ multimodal imaging methodology was developed to reveal the origin of recombination among locally-confined carriers and to bridge microscopic microstructure modulation with macroscopic emission properties for InGaN-based red LEDs.

Experiments

Epitaxial growth and device fabrication

InGaN MQWs were epitaxially grown on (111) silicon substrates using metalorganic chemical vapor deposition (MOCVD). The growth of epitaxial structure was initiated by an AlN nucleation layer and step-graded AlGaN buffer layers. Figure 1a illustrates the schematic epitaxial structures, with the growth procedure terminating at the active region. Following the growth of an *n*-GaN layer, 520 nm non-intentionally doped GaN, and 10 pairs of superlattices (SLs), the active region were grown. As shown in Fig. 1d, the active region of red LEDs consists of five pairs of MQWs composed of 3- nm-thick $In_{0.3}Ga_{0.7}N$ QWs and AlN/GaN heterogeneous quantum barriers (QBs). After selective etching, the *n*-electrodes were deposited on the via holes. Then, the epitaxial wafer was bonded onto a (100) silicon substrate through eutectic bonding. Next, the epitaxial substrate was removed by chemical mechanical polish (CMP) and wet etching, the flipped structures were etched by inductively coupled plasma reactive ion etching (ICP-RIE), first removing bottom layers and 2.5 μm thick *n*-GaN layer, and selectively etching to form mesa of red LEDs. Following these steps, a SiO_2 passivation layer was deposited using plasma-enhanced chemical vapor deposition (PECVD), with subsequent deposition of the Ni/Au metal layers as contact electrodes in Fig. 1c. As shown in Figure S1, InGaN-based red LEDs with an edge length of 300 μm were fabricated. The red

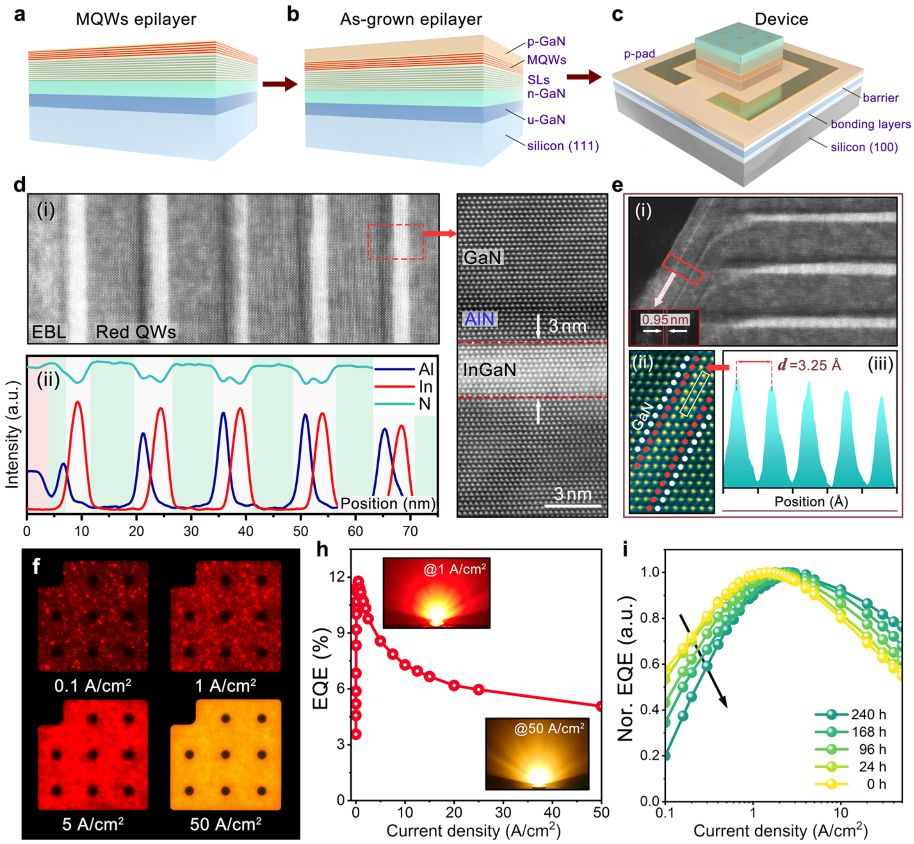

Fig. 1 **a** Schematic epitaxial structures of InGaN red MQWs grown on the silicon substrate. **b** As-grown epitaxial layers with *p*-GaN layers. **c** Schematic illustration of InGaN-based red LEDs. **d** STEM images of InGaN-based QW/QB layers, and corresponding elemental distribution diagram. **e** Cross-sectional STEM image of a V-pit structure and its magnified atom-resolved STEM image, intensity profile of QWs, and the corresponding atomic distance. **f** Photographs of red LEDs under different current density. **h** EQE as a function of the current density at 300 K. Inset shows the EL images at 1 and 50 A/cm^2, respectively. **i** Normalized EQE curves of InGaN-based red LEDs after different aging durations (under 50 ℃ and 50% humidity)

micro-LEDs were fabricated on the silicon substrate by processes similar to our previous work [9].

Characterization

The electrical characteristics of devices were measured by using a current–voltage source (GS610, Yokogawa). The photoluminescence (PL) and electroluminescence (EL) spectral characteristics were measured by a spectrometer (QE65Pro, Ocean Optics) coupled to an optical fiber, and the temperature-dependent measurements were conducted in a closed cycle cryostat (CS202-DMX, ARS). The surface morphology of MQWs was characterized using scanning electron microscopy (SEM, Solaris, TESCAN) and atomic force microscopy (AFM, Dimension FastScan, Bruker). Figure S2 shows the AFM and SEM images of the red MQWs grown on the silicon substrate, the surface morphology comprises the relative flat plane and inverted hexagonal pyramid pits, the depth of V-pits is approximately 140 nm, and the V-pit density is calculated to be $\sim 1.22 \times 10^9$ cm^{-2}, which are larger than those of the MQWs grown on sapphire substrates [25–27].

Cross-sectional specimens of MQWs and V-pits were fabricated by focused-ion-beam (FIB). The cross-sectional transmission electron microscopy (STEM) image of QW/QB layers and the corresponding elemental distribution diagram are shown in Fig. 1d. The spatially-resolved confocal μ-PL measurement was carried out by using fluorescence spectrometer (FluoMic and FluoTime 300, PicoQuant, excitation laser: 405 nm, ~ 3.07 eV), μ-EL measurement was performed using a hyperspectral camera (GaiaField-F-V10, Dualix). The epi-layers and devices under test were mounted onto a temperature controller set at 300 K, and the spatial resolution of the system is approximately 0.27 μm. Spatially-resolved cathodoluminescence (CL) imaging was carried out using a CL spectrometer (SPARC Spectral, Delmic) with a spectral resolution of about 0.42 nm and a spatial resolution of approximately 20 nm.

Results and discussion

As illustrated in Fig. 1d, five distinct bright horizontal stripes corresponding to QWs can be clearly observed in the planar region of the microstructure. In contrast, in Fig. 1e, the thickness of the inclined QWs is narrower at the semipolar sidewall region, measuring approximately 0.95 nm, which is about one-third of the thickness of the planar wells. The indium content in the sidewall of V-pits is less than that in the planar QWs, and the atomic distance of InGaN within the inclined QWs region is 3.25 Å measured from the distance-dependent contrast in the atom-resolved image.

Subsequently, the as-grown epilayers (with *p*-GaN) were further processed to fabricate the devices, Fig. 1f displays the direct observation of the EL images from the fabricated devices, wherein the light-emitting patterns of LEDs exhibit a blueshift from red to amber or even yellow. The InGaN-based red LEDs exhibit apparent localized emission under lower current density, Fig. 1h reveals that devices achieve peak EQE of 11.78%. In Figure S3c, after accelerated aging under 50℃, 50% humidity, and 50 A/cm^2 DC driving, we can observe that the maximum EQE decreases to 8.25% (70% to its initial value) at 192 h and 6.96% at 240 h. Afterwards, the current density dependence of EQE was normalized to its maximum value in Fig. 1i, the rising component of the EQE curve descends with the increase of aging time, indicating the intensification of Shockley–Read–Hall (SRH) non-radiative recombination; this can be attributed to traps assisted tunnels (TAT) in deep defects [28].

Figure 2a shows the CL spectrum of red MQWs, featuring four characteristic peaks at approximately 360, 425, 500, and 575 nm, respectively. Spatially-resolved CL mappings at these wavelengths are presented in Fig. 2b. The bright spots observed at 360, 425, and 500 nm emissions align closely with the V-pit distribution and can be ascribed to the near-band-edge (NBE) emission from the GaN layers, emission from thinner inclined MQWs and ultrathin SLs within the V-pits [29, 30], and the intensity of these super-bandgap emission peaks is significantly attenuated outside V-pits. However, the 575 nm emission predominantly occurs within the discrete regions surrounded by the V-pits, this can be explained by the shielding effect of dislocations [26, 31]. As shown in Figs. 2d-e, the intensity of the 575-nm peak outside the V-pit is significantly enhanced with an increase in accelerated voltage (V_{acc}) from 4 to 8 kV, while the maxima at 425 and 500 nm show an increase inside the V-pit. However, within the V-pit region, the point-by-point scanning CL intensity

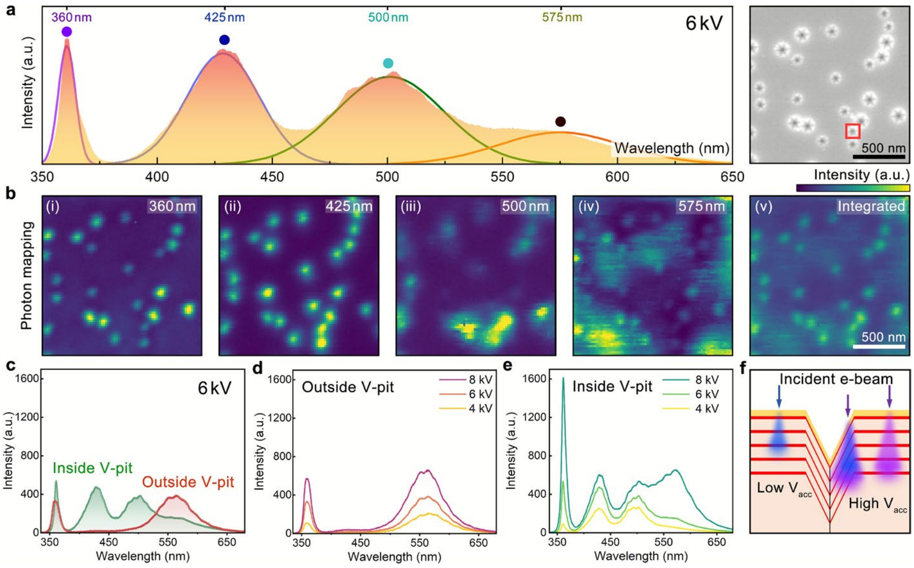

Fig. 2 **a** CL spectrum of a V-pit microstructure (indicated by red square in the SEM image) of the InGaN red MQWs (epi-layers) under an acceleration voltage of 6 kV. **b** Spatially-resolved CL mappings at featured wavelengths of 360, 425, 500, and 575 nm, and corresponding integrated intensity mapping. **c** CL spectra of the V-pit region and its surrounding region under an acceleration voltage of 6 kV. CL spectra under different voltage for **d** V-pit region and **e** V-pit surrounding region. **f** Schematic diagram of incident beam trajectories and CL penetration depth with increasing acceleration voltage in V-pit region and its surrounding region

of the characteristic peak at 575 nm gradually increases when V_{acc} exceeds 4 kV, which can be explained by the parasitic light emission from the planar QWs owing to the expansion of the excitation width of incident beam with increasing penetration depth (see Fig. 2f) [32, 33].

In-situ spatially-resolved hyperspectral imaging can be utilized through microscopic metrologies to directly demonstrate carrier behaviors within the microstructure of the active region. Figure 3a shows the spatially-resolved PL mappings of epi-layers, revealing discrete localized emission patterns under low PL excitation density, whereas these PL patterns become more uniform with increasing excitation intensity. Figure 3b presents time-resolved photoluminescence (TRPL) from the featured bright and dark regions, with the biexponential function employed to fit the TRPL curves, expressing as follows [34]

$$I(t) = A_1 e^{-\frac{t}{\tau_1}} + A_2 e^{-\frac{t}{\tau_2}} \tag{1}$$

where A_1 and A_2 denote the TRPL intensity coefficients, and τ_1 and τ_2 are the time constants of PL decay. As shown in Fig. 3b and Table S1, the short component τ_1 within the dark region (2.30 ns) is less than that in the bright region (4.17 ns), which can be associated to the carrier transport from the semipolar inclined MQWs in V-pits to planar MQWs [35]. Whereas, the long component τ_2 of dark region exceeds that of bright region, which indicates the relatively lower probability of radiative recombination [36]. The transient rise time (τ_0) is 0.60 ns in the dark region and 1.60 ns in the bright region, respectively. The fast rise portion in the dark region can be attributed to the carrier relaxation in quantum wells. However, the relatively slow transient rise in the bright

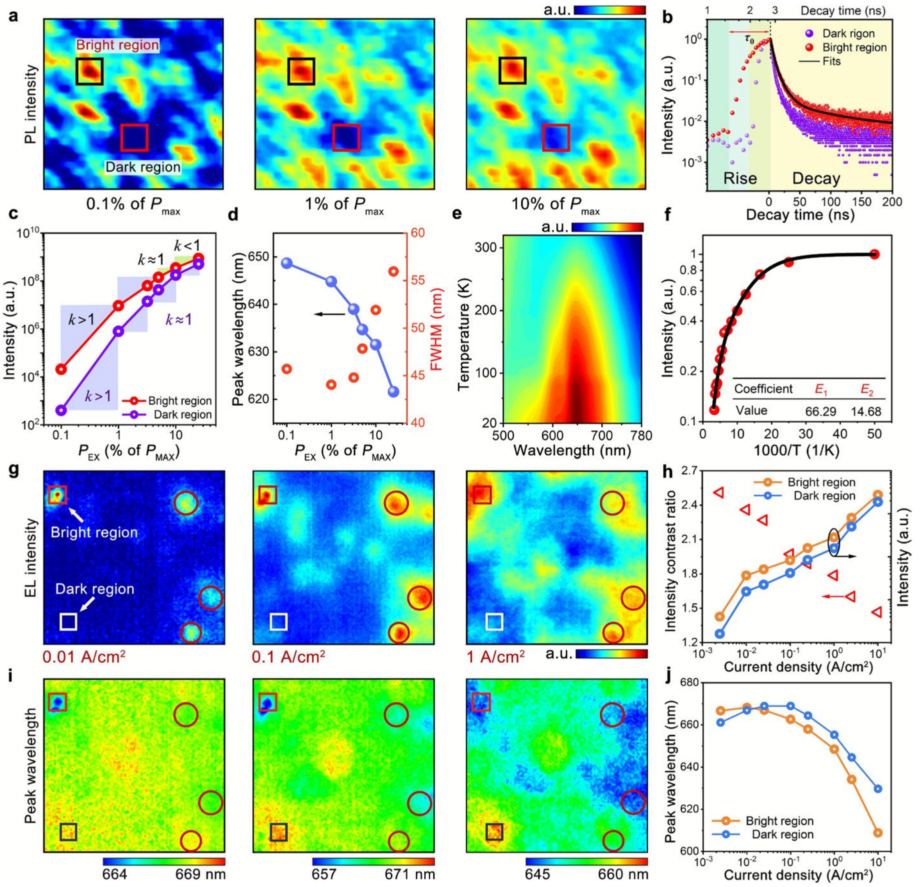

Fig. 3 **a** Confocal PL intensity mappings under different laser excitation intensity: 0.1%, 1%, and 10% of the maximum power, scale: 6.8 μm × 6.8 μm. **b** TRPL curves of the bright and dark regions at 630 nm. **c** Integrated PL intensity as a function of the excitation power. The parameter *k* refers to the slope of the P_{EX}-P_{Int} curve under double-exponential plot. **d** Peak wavelength and FWHM as a function of the excitation power in the bright PL region. **e** Pictorial views of temperature-dependent logarithmic PL spectra, and **f** corresponding normalized integrated PL intensity as a function of the temperature. Excitation power: 10 mW. **g** Spatially-resolved mapping of EL intensity of red LEDs at 300 K under the current density of 0.01, 0.1, and 1 A/cm^2, respectively, map scale: 10 μm × 10 μm. **h** Average EL intensity in the bright and dark regions and intensity contrast ratio I_{bright}/I_{dark} as a function of the current density. **i** Spatially-resolved mapping of the fitted peak wavelength at the current density of 0.01, 0.1, and 1 A/cm^2, respectively. **j** Current density-dependent peak wavelength in two regions

region can be associated with the thermionic interwell hole transport [36, 37], indicating that the existent of hole injection through the sidewall of V-pits. The dimensions of these bright regions are comparable to that in the CL results, implying that those regions are associated to the planar MQW regions [34, 38]. Figure S5 shows the spatially resolved distribution of time-resolved CL (TRCL) lifetime in a V-pit region, the value of short component (τ_{C1}) is significantly smaller in pixels corresponding to the region of V-pit (about 200 ps). In contrast, the lifetime mapping of long component (τ_{C2}) shows a complementary trend at the inclined sidewall of V-pits (in the range of 6.8 ~ 7.0 ns), which is consistent with the TRPL.

Figure 3c presents the excitation-dependent integrated PL intensity, revealing the contrast ratio between the two regions diminishes as the excitation power increases.

Nevertheless, despite this reduction in PL intensity contrast, the locally enhanced emissions remain clearly distinguishable on the intensity mapping. The PL excitation-emission curves can be further differentiated as sub-linear region ($k > 1$), linear region ($k \approx 1$), and super-linear region ($k < 1$), representing that carrier dynamics is dominated by SRH nonradiative recombination, radiative recombination, and Auger recombination [26], respectively. Since Auger recombination requires locally high density of carriers, the absence of Auger recombination features in dark region suggests that the carriers mainly dissipated through SRH nonradiative recombination in V-pits. Figure 3d shows the blueshift in PL spectra, and a decrease-increase trend of FWHM with increasing excitation density, which can be attributed to the Coulomb screening of polarized electric field and band-filling effect, respectively [39].

Figures 3e-f illustrate the PL results at different temperatures, showing that the PL intensity progressively declines with increasing temperature, which can be attributed to thermal quenching [40]. The temperature dependence of the integrated PL intensity (Arrhenius plots) was recorded from cryogenic temperatures to 300 K and normalized to its maximum value at 20 K. At 300 K. The evolution of internal quantum efficiency (IQE) with excitation PL intensity is calculated by different-excitation-power PL method [41], resulting in maximum IQE of 51.8% in Figure S8. The thermal activation process of InGaN red MQWs can be described by [42]

$$I(T) = \frac{I_0}{1 + C_1 \exp\left(-\frac{E_1}{k_B T}\right) + C_2 \exp\left(-\frac{E_2}{k_B T}\right)} \tag{2}$$

where I_0 is the PL intensity at the lowest measured temperature, C_1 and C_2 are rate constants, E_1 and E_2 denote the activation energy for SRH nonradiative recombination and carrier scattering process from localization, and k_B is the Boltzmann's constant. E_1 is determined to be 66.29 ± 5.79 meV, which is comparable to the activation energy for thermal quenching of carrier recombination. However, E_2 is 14.68 ± 0.63 meV, indicating that the extent of localized confinement is more pronounced at cryogenic temperatures.

The in-situ hyperspectral EL mappings at a scale of 10 μm × 10 μm under varying current densities are depicted in Fig. 3g. Similar to the PL results, the spot-like local emissions are prominent under lower carrier injection levels and gradually expand to encompass surrounding regions as the current density increases. Figure 3h exhibits the average integrated EL intensity in the featured bright and dark regions, and the EL intensity ratio between these regions (i.e., the region intensity contrast ratio, defined as $I_{\text{bright}}/I_{\text{dark}}$) gradually decreases from 2.51 at 2.5×10^{-3} A/cm^2 to 1.47 at 10 A/cm^2. In Fig. 3i, the mapping of the peak wavelength also reveals spatial nonuniformity under different current density, the regions with strong local EL emission showing a high degree of positive correlation with the regions exhibiting a blueshift in the peak wavelength. The current density-dependent peak wavelengths in the bright and dark regions are shown in Fig. 3j. The peak wavelength of the bright region shifts from 667 to 648 nm as the current density increases from 2.5×10^{-3} to 1 A/cm^2. In contrast, the peak wavelength of the dark region initially redshifts from 661 nm at 2.5×10^{-3} A/cm^2 to 669 nm at 0.1 A/cm^2, before subsequently shifting to 655 nm at 1 A/cm^2. Figure S6 shows the current density dependent-peak energy and FWHM, indicating that the decrease of emission energy with increasing current density is attributed to the redistribution of localized carriers. The peak wavelength deviation between bright and dark regions within the inspected micro-regions reaches approximately 7 nm at 1 A/cm^2 and even 21 nm at 10 A/cm^2, suggesting that the bright regions possess stronger band-filling effect due to the locally confined carriers.

Accordingly, the temperature-dependent normalized EL spectra are shown in Fig. 4a. As the temperature increases from 20 to 300 K, the peak wavelength gradually blueshifts under typical current density (0.01, 0.1, and 1 A/cm^2). The variation of peak wavelength with temperature is the result of the interplay between localized carrier thermalization and bandgap shrinkage [43], a larger extent of localization can lead to more significant blueshift in peak wavelength, resulting from the dominance of carrier thermalization from localized states, where delocalized carriers occupy higher energy levels. However, the impact of localization is gradually weakened with the increase of current density, and the contributions of these two factors are comparable, thus, the peak wavelength is less dependent with temperature [44]. The inspection of the temperature-dependent normalized spectra is presented in Figure S7. Spectral broadening occurs on the high-energy side of EL spectra as the temperature rises from 20 to 300 K, suggesting increased recombination from higher energy states. Figure 4b shows the temperature dependence of the EL spectra at an injection density of 1 A/cm^2. The thermal quenching observed in EL intensity follows an increasing–decreasing trend with rising temperature, which can be attributed to carrier loss via localization at cryogenic temperatures, as discussed in previous studies [45, 46]. There are apparent differences among the spectra collected under CL, PL, and EL. For CL, the photons were excited by electron beam (acceleration voltage 4 to 8 keV), which have larger energy than the bandgap of GaN (super-bandgap absorption), thus, the spectra contain the emission from GaN and InGaN. Since the photon energy of the PL excitation laser lies between bandgap energies of the barrier and the well layers, the photons are resonantly absorbed by the active layer, *electron–hole* pairs are exclusively generated in QWs not in GaN. For EL, the recombination of carriers occurs in QWs.

The numerical analysis of V-pit microstructures in InGaN-based red LEDs was also carried out by Crosslight APSYS. The simulation results in Fig. 4c show that the hole concentration in the external planar QWs is higher than that in the inclined QWs [47], and simultaneously, that concentration within the inclined QWs shows a significant difference, which is 4.8×10^{10} cm^{-3} ($p_{\mathrm{QW5\_}h}$) in QW5 and 1.6×10^{19} cm^{-3} ($p_{\mathrm{QW1\_}h}$) in QW1. Accordingly, Fig. 4h shows the concentration distribution of electron (or hole) in the V-pit inclined region, which, following a stepwise upward (or downward) change. There is a significant disparity between electron and hole concentrations in the QWs, and the radiative recombination rate in the QWs is mainly determined by hole concentration (p_{QW}), electron concentration (n_{QW}), and radiative recombination coefficient (B). In the inclined QW1, the electron concentration ($n_{\mathrm{QW1\_}e} = 2.9 \times 10^9$ cm^{-3}) is less than the hole concentration ($n_{\mathrm{QW1\_}h} = 1.6 \times 10^{19}$ cm^{-3}), while in the inclined QW5, those are $p_{\mathrm{QW5\_}e} = 8.6 \times 10^{18}$ cm^{-3} and $p_{\mathrm{QW5\_}h} = 4.8 \times 10^{10}$ cm^{-3}. Therefore, as shown in Fig. 4d and Table S3, the radiative recombination rate in the inclined QW5 should be higher than that in inclined QW1, owing to its significantly higher electron concentration. The calculation results in Fig. 4i show a reduction in

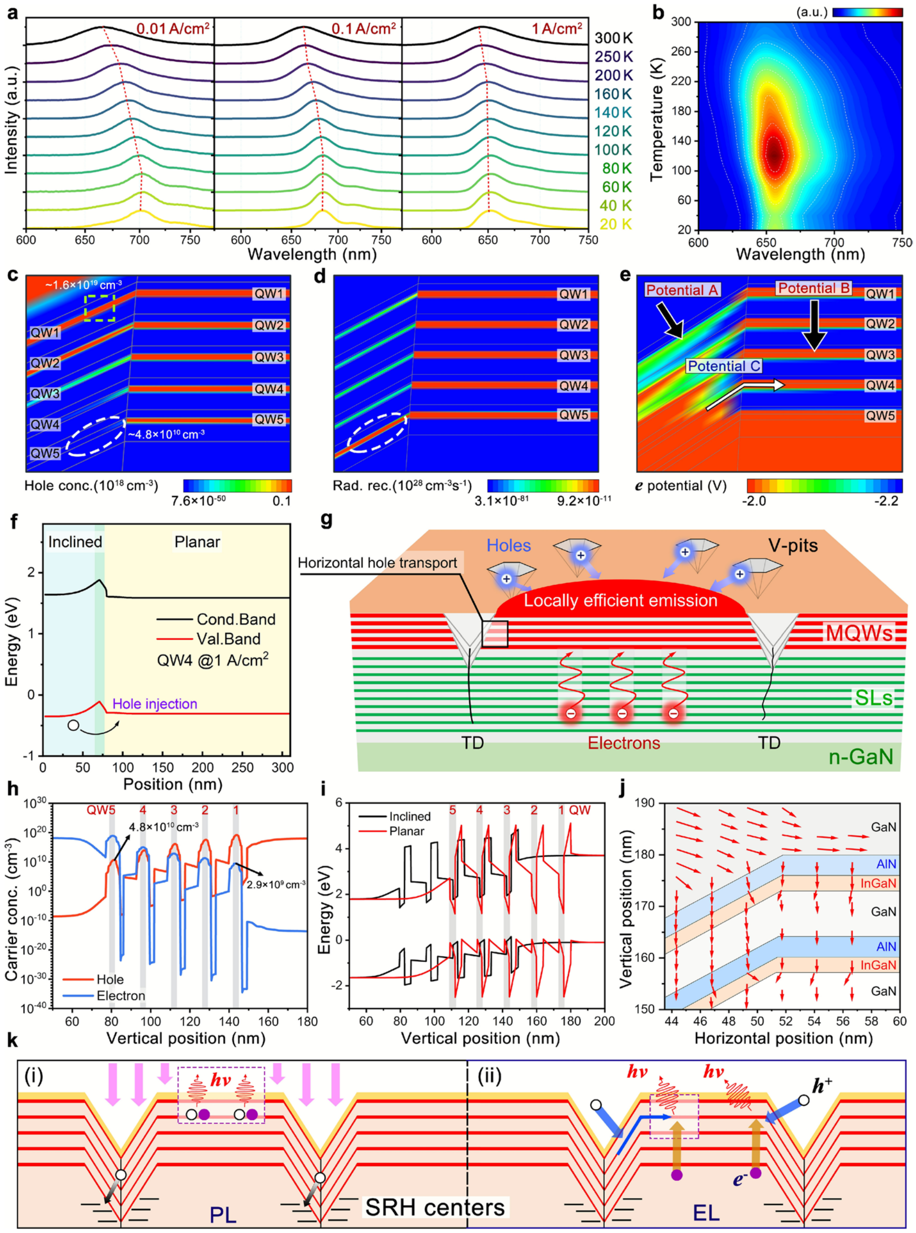

Fig. 4 **a** Temperature-dependent EL spectra of device at 0.01, 0.1, and 1 A/cm^2. **b** Pictorial views of temperature-dependent EL spectra at 1 A/cm^2. **c** The calculated 2D hole concentration distribution, **d** 2D radiative recombination rate distribution, and **e** 2D negative (electron) potential distribution of MQWs with the V-pit microstructure at 1 A/cm^2. The directions of positive (hole) potentials are indicated by Potential A/B/C. **f** Band profiles along the direction indicated by Potential C at 1 A/cm^2. **g** Schematic diagram of the formation of three-dimensional hole injection pathways around V-pits. **h** Carrier concentration (along vertical direction) of QWs in the inclined sidewall of the V-pit at 1 A/cm^2. **i** Energy band structure diagram (along vertical direction) of LEDs in the planar region and the V-pit region at 1 A/cm^2. Vertical position: Bottom-to-top. **j** Simulated current vectors in the MQWs with V-pit microstructure at 1 A/cm^2. **k** Schematic diagrams of carrier recombination under PL and EL modes

the polarization effect in the inclined QWs, which leads to higher energy emission from the inclined QWs.

The carrier dynamics in the semipolar sidewall of V-pits is governed by the inhomogeneous distribution of the electric field in the V-pit microstructure. As shown in Fig. 4j, the simulated current vectors indicate that holes can efficiently inject into the planar QWs through the sidewalls of V-pits. Therefore, the devices with a rational V-pit distribution can enhance the current injection efficiency (η_{inj}), thereby achieving higher EQE under EL [36, 48]. Consequently, it can be inferred that efficient local carrier injection facilitates highly efficient red emission in the In-rich QWs. Herein, a reverse bias was applied on the simulated structure, the 2D electron potential distribution (in contrast to the hole potential) of the active layers is illustrated in Fig. 4e, where the hole potentials in the *p*-GaN layer are higher in both the planar and V-pit regions compared to those in the active layers. Therefore, the electric field should be directed vertically in the planar region and in the inclined direction in the V-pit region (Potential A and Potential B). In addition, within the QWs, the potential along the inclined sidewall of the V-pit is always higher than that in the planar region (Potential C). As shown in Fig. 4f, the band profiles along the direction indicated by Potential C in Fig. 4e show remarkable energy difference between the semipolar inclined QW and planar QW. Holes can drift from the inclined QWs into the planar QWs, thereby forming a two-stage hole injection pathway [35].

Based on the discussion provided above, the V-pit engineering can create three-dimensional current injection pathways vertical to the inclined sidewall surrounded by V-pits, i.e., the injected holes are locally confined and efficiently transported from semipolar to polar QWs under electrical injection conditions (see Fig. 4g). Figure 4k illustrates the possible carrier recombination mechanisms under different excitation modes. Under PL excitation, resonant absorption of excitation photons in MQWs allows radiative recombination of carriers in active layers, while the carriers within V-pit may be trapped by the nonradiative centers. However, for EL, the recombination of electrons and holes preferentially occurs in the planar MQWs surrounded by V-pits due to the efficient hole injection at the semipolar sidewall of V-pits. Our findings from microscopic hyperspectral imaging, including CL, PL, and EL measurements, suggest that the planar region surrounded by V-pits can obtain enhanced hole injection and improved radiative recombination.

The InGaN-based 10 μm red micro-LEDs were demonstrated using the same epitaxial layers (Fig. 1b). As shown in Fig. 5a, the EQE curve initially exhibits a sharp rising edge, followed by a pronounced concave efficiency droop at high current densities [49]. The 10 μm micro-LEDs achieve a maximum on-chip EQE of 1.10% at 0.1 A/cm^2 at 300 K. Figure 5c shows the peak EQE of InGaN-based red micro-LEDs grown on silicon substrates as reported in previous studies [8, 9, 17, 18, 50–52], without additional packaging processes. The values are less than those of devices grown on sapphire or patterned sapphire substrates (PSS), which can be partly attributed to the light absorption of substrate and the on-wafer architecture. Here, the characteristic temperature (T_C) of red micro-LEDs is examined; a higher T_C is desirable for demonstrating temperature stability of the device and indicating the mitigation of nonradiative recombination. Inset in Fig. 5a shows the characteristic temperature (T_C) of the red micro-LEDs, which can be deduced from [53]

$$\frac{L}{L_0} = \exp\left(-\frac{T - 300\mathrm{K}}{T_C}\right) \tag{3}$$

where L is the light output power (LOP) and L_0 denotes the LOP at 300 K. Hence, the LOP values of micro-LEDs are normalized, and T_C is obtained to be 86 K at 0.1 A/cm^2, 139 K at 1 A/cm^2, and 221 K at 10 A/cm^2. Moreover, the redshift coefficient, suggesting

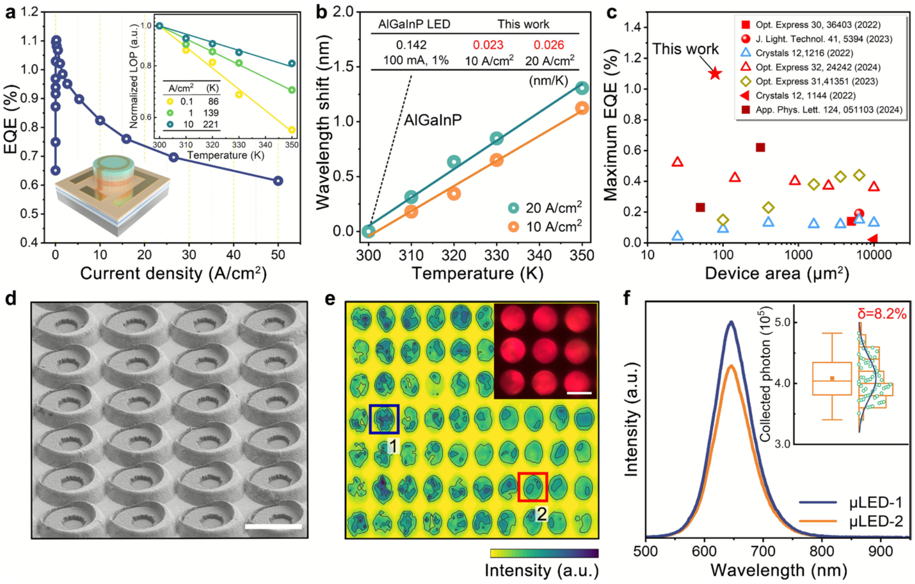

Fig. 5 **a** Current density as a function of EQE for the 10 μm red micro-LEDs. Inset shows the schematic illustration of InGaN-based red micro-LEDs and temperature dependence of normalized LOP and corresponding characteristic temperature (T_C). **b** Temperature-dependent wavelength shift. **c** Benchmark of maximum EQE as a function of the device size for InGaN-based red micro-LEDs grown on silicon substrates. Solid and open symbols are InGaN-based micro-LEDs with wavelengths longer and shorter than 630 nm at the peak EQE, respectively. **d** Bird's-eye view SEM image of the red micro-LEDs. **e** Microscopic hyperspectral image of the micro-LED array. Inset shows the microscopic EL image of red micro-LEDs. **f** EL spectra (at 1 A/cm^2) from the selected micro-LEDs in the array. Inset illustrates the EL intensity distribution of the micro-LEDs in the array

the extent of temperature-induced wavelength redshift, is provided in Fig. 5b. The coefficient can be calculated by [54]

$$\text{Redshift Coefficient} = \frac{\lambda - \lambda_0}{T - T_0} \tag{4}$$

where T_0 is 300 K and λ_0 is the peak wavelength at 300 K [55]. The obtained redshift coefficients are 0.023 nm/K at 10 A/cm^2 and 0.026 nm/K at 20 A/cm^2. This is comparatively superior to the AlGaInP-based red micro-LEDs, suggesting that the InGaN-based red micro-LEDs exhibit limited wavelength shifts when operating across a wide temperature range [55, 56]. Figure S9b presents the *I-V* curve of micro-LEDs. The red micro-LEDs array is demonstrated in Fig. 5d, and the EL emission hyperspectral image of the red micro-LED array at 10 A/cm^2 is shown in Fig. 5e, followed by an inspection on the spatially-resolved emission from the micro-LED array achieved through extraction of local spectra from individual micro-LEDs. The luminance nonuniformity in the micro-LED array can be attributed to the nonuniform V-pit distribution and hole injection. The spectra are depicted in Fig. 5f, where the EL uniformity estimation of the fabricated array is 8.2%, with a peak wavelength difference among micro-LEDs of 1.61 nm (shown in Figure S10).

Conclusion

In summary, this work provides a thorough investigation into the impacts of V-pit microstructures on the performance of in InGaN-based red LEDs grown on silicon substrates. Efficient local emission from red MQWs can be achieved by reasonably modulating the V-pit density, which significantly enhances local hole injection efficiency. The InGaN-based red LEDs exhibit a peak EQE of 11.78%, the on-chip maximum EQE of 10 μm micro-LEDs reaches 1.10% at 0.1 A/cm^2 at 300 K. The efficiency of red LEDs can maintain at 70% to its initial value after 192 h accelerated aging at 50℃, 50% humidity. Characteristic temperature and redshift coefficient of red micro-LEDs are obtained to be 221 K and 0.023 nm/K at 10 A/cm^2. Insights from this study suggest that V-pit-modulated InGaN MQWs can offer advantages for long-wavelength micro-LEDs and potentially for micro-displays.

Supplementary Information

The online version contains supplementary material available at https://doi.org/10.1186/s43074-025-00214-2.

Supplementary Material 1: Figure S1. Fabrication process of InGaN-based LEDs. Figure S2. Morphological characterization of V-pit on the MQWs. Figure S3. EQE as a function of current density. Table S1 & Figure S4. TRPL and μ-TRPL results. Figure S5. TRCL lifetime mapping. Figure S6. Current density versus peak energy and FWHM. Figure S7. Temperature-dependent normalized EL spectra of devices. Figure S8. Power-dependent PL measurements. Figure S9. Current density–voltage curves of devices and micro-LEDs. Table S2. Fitting Arrhenius parameters. Table S3. Simulation results of QWs. Figure S10. Peak wavelength position distribution. Figure S11. EL spectra and CIE coordinates. Figure S12. EQE droop and temperature-dependent wavelength shift; Table S4: Redshift coefficient of InGaN-based red LEDs. Table S5. Comparison of long-wavelength InGaN-based LEDs.

Acknowledgements

H.V. Demir gratefully acknowledges support from TUBA-The Turkish Academy of Science. The authors acknowledge Tianjin SimuCal Technology Co., Ltd. for valuable discussion.

Authors' contributions

Conceptualization: Xi Zheng and Weijie Guo; Project administration: Weijie Guo, Yi Fu, Tingzhu Wu, Hilmi Volkan Demir, and Zhong Chen; Supervision: Weijie Guo, Yijun Lu, Tingzhu Wu, and Zhong Chen; Funding acquisition: Weijie Guo and Zhong Chen; Validation: Xi Zheng and Guobao Zhao; Methodology: Xi Zheng, Yi Fu, Mingbing Zhou, Tao Huang, Swee Tiam Tan, Yijun Lu, and Tingzhu Wu; Resources: Yurong Dai, Yi Fu, Tao Huang, and Vijay Kumar Sharma; Investigation: Guobao Zhao, Yurong Dai, Yi Fu, Mingbing Zhou, and Tao Huang; Data Curation: Xi Zheng and Yurong Dai; Formal analysis: Xi Zheng, Guobao Zhao, and Swee Tiam Tan; Software: Mingbing Zhou, Vijay Kumar Sharma; Visualization: Xi Zheng and Yurong Dai; Writing – original draft: Xi Zheng, Weijie Guo, and Guobao Zhao; Writing – review & editing: Xi Zheng, Weijie Guo, Guobao Zhao, Swee Tiam Tan, Vijay Kumar Sharma, Hilmi Volkan Demir, and Zhong Chen.

Funding

This work was supported in part by the National Natural Science Foundation of China under Grant 62474149, in part by the Science and Technology Project of Fujian Province under Grant 2023H6038, in part by the Fujian Provincial Natural Science Foundation of China under Grant 2024J01052, in part by the Suzhou Integrated Circuit Advanced Packaging Substrate Technology Innovation Consortium under Grant LHT202329, in part by the Xiamen Science and Technology Plan Project under Grant 3502Z20241021.

Data availability

Data will be available on reasonable request.

Declarations

Competing interests

The authors declare that they have no competing interests.

Received: 13 August 2025 Revised: 24 November 2025 Accepted: 4 December 2025

Published online: 16 December 2025

References

1. Behrman K, Kymissis I. Micro light-emitting diodes. Nat Electron. 2022;5(9):564–73.

2. Baek W, Park J, Shim J, Kim B, Park S, Kim H, et al. Ultra-low-current driven InGaN blue micro light-emitting diodes for electrically efficient and self-heating relaxed microdisplay. Nat Commun. 2023;14:1386.
3. Park J, Choi JH, Kong K, Han JH, Park JH, Kim N, et al. Electrically driven mid-submicrometre pixelation of InGaN micro-light-emitting diode displays for augmented-reality glasses. Nat Photon. 2021;15(6):449–55.
4. Song Y, Yuan J, Chen Q, Liu X, Zhou Y, Cheng J, et al. Three-dimensional varifocal meta-device for augmented reality display. PhotoniX. 2025;6(1):6.
5. Zhuang Z, Iida D, Velazquez Rizo M, Ohkawa K. 630-nm red InGaN micro-light-emitting diodes (<20 μm × 20 μm) exceeding 1 mW/mm^2 for full-color micro-displays. Photonics Res. 2021;9(9):1796–802.
6. Flemish J, Armitage R, Ren Z, Soer W, Lotfi H, Chung T, et al. 38-3: Invited paper: MicroLED device technology for low-power wearable displays. SID Symp Dig Tech Pap. 2022;53(1):478–80.
7. Armitage R, Ren Z, Holmes M, Flemish J. True-red InGaN light-emitting diodes for display applications. Phys Status Solid Rapid Res Lett. 2024;18(11):2400012.
8. Lu X, Li Y, Jin Z, Zhu S, Wang Z, Qian Z, et al. Red InGaN micro-LEDs on silicon substrates: potential for multicolor display and wavelength division multiplexing visible light communication. J Lightwave Technol. 2023;41(16):5394–404.
9. Zheng X, Xu X, Tong C, Fu Y, Zhou M, Huang T, et al. Chromatic properties of InGaN-based red, green, and blue micro-LEDs grown on silicon substrate. Appl Phys Lett. 2024;124(5):051103.
10. Lin CC, Wu YR, Kuo HC, Wong MS, DenBaars SP, Nakamura S, et al. The micro-LED roadmap: status quo and prospects. J Phys Photonics. 2023;5(4):042502.
11. Qian Y, Yang Z, Chen SC, Ma Y, Chen YC, Chen HS, et al. Power consumption of light engines for emerging augmented reality glasses: perspectives and challenges. Adv Photon. 2025;7(3):034001.
12. Li P, Ewing J, Wong MS, Yao Y, Li H, Gandrothula S, et al. Advances in InGaN-based RGB micro-light-emitting diodes for AR applications: status and perspective. APL Mater. 2024;12(8):080901.
13. Zheng Y, Chu F, Lin F, Hu Y, Li Y, Zheng Y, et al. Wide-viewing-angle color holographic 3D display system with high brightness encoding. PhotoniX. 2025;6(1):3.
14. Li P, Li H, Yao Y, Lim N, Wong M, Iza M, et al. Significant quantum efficiency enhancement of InGaN red micro-light-emitting diodes with a peak external quantum efficiency of up to 6%. ACS Photonics. 2023;10(6):1899–905.
15. Chen Z, Sheng B, Liu F, Liu S, Li D, Yuan Z, et al. High-efficiency InGaN red mini-LEDs on sapphire toward full-color nitride displays: effect of strain modulation. Adv Funct Mater. 2023;33(26):2300042.
16. Yu L, Hao Z, Luo Y, Sun C, Xiong B, Han Y, et al. Improving performances of ultra-small size (1–20 μm) InGaN red micro-LEDs by growing on freestanding GaN substrates. Appl Phys Lett. 2023;123(23):232106.
17. Ewing J, Lynsky C, Zhang J, Shapturenka P, Wong M, Smith J, et al. Influence of superlattice structure on V-defect distribution, external quantum efficiency and electroluminescence for red InGaN based μLEDs on silicon. Crystals. 2022;12(9):1216.
18. Park J, Youn EJ, Baek WJ, Chu EK, Kim HS, Geum DM, et al. Size-dependent optoelectronic characteristics of InGaN/GaN red micro-LEDs on 4-inch Si substrates: high pixel density arrays demonstration. Opt Express. 2024;32(14):24242–50.
19. Li P, Li H, Zhang H, Lynsky C, Iza M, Speck JS, et al. Size-independent peak external quantum efficiency (>2%) of InGaN red micro-light-emitting diodes with an emission wavelength over 600 nm. Appl Phys Lett. 2021;119(8):081102.
20. Zhuang Z, Iida D, Ohkawa K. Ultrasmall and ultradense InGaN-based RGB monochromatic micro-light-emitting diode arrays by pixilation of conductive p-GaN. Photonics Res. 2021;9(12):2429–34.
21. Shi Z, Tian A, Sun X, Li X, Zang H, Su X, et al. Formation mechanism of trench defects in green InGaN/GaN multiple quantum wells. J Appl Phys. 2023;133(12):123103.
22. Wu H, Lin X, Shuai Q, Zhu Y, Fu Y, Liao X, et al. Ultra-high brightness micro-LEDs with wafer-scale uniform GaN-on-silicon epilayers. Light Sci Appl. 2024;13:284.
23. Hu F, Chen S, Zhang Y, Li G, Zou P, Zhang J, et al. High-speed visible light communication systems based on Si-substrate LEDs with multiple superlattice interlayers. PhotoniX. 2021;2(1):16.
24. Laryn T, Chu RJ, Kim Y, Ju E, Ahn C, Yu H-Y, et al. Multifunctional metamorphic III-V distributed Bragg reflectors grown on Si substrate for resonant cavity surface emitting devices. PhotoniX. 2025;6(1):21.
25. Zhang S, Zhang J, Gao J, Wang X, Zheng C, Zhang M, et al. Efficient emission of InGaN-based light-emitting diodes: toward orange and red. Photonics Res. 2020;8(11):1671–5.
26. Pan Z, Chen Z, Zhang H, Yang H, Deng C, Dong B, et al. Efficient InGaN-based red light-emitting diodes by modulating trench defects. Adv Funct Mater. 2024;34(25):2315781.
27. Liu Y, Wang G, Feng F, Zhanghu M, Yuan Z, Li Z, et al. Ultra-low-defect homoepitaxial micro-LEDs with enhanced efficiency and monochromaticity for high-PPI AR/MR displays. PhotoniX. 2024;5(1):23.
28. Mandurrino M, Goano M, Vallone M, Bertazzi F, Ghione G, Verzellesi G, et al. Semiclassical simulation of trap-assisted tunneling in GaN-based light-emitting diodes. J Comput Electron. 2015;14(2):444–55.
29. Finot S, Le Maoult C, Gheeraert E, Vaufrey D, Jacopin G. Surface recombinations in III-nitride micro-LEDs probed by photon-correlation cathodoluminescence. ACS Photonics. 2022;9(1):173–8.
30. Alreshidi F, Chen LR, Najmi M, Xin B, Alamoudi H, Melinte G, et al. Enhanced efficiency InGaN/GaN multiple quantum well structures via strain engineering and ultrathin subwells formed by V-pit sidewalls. ACS Appl Opt Mater. 2024;2(1):220–9.
31. Zhan J, Chen Z, Deng C, Jiao F, Xi X, Chen Y, et al. A novel way to fill green gap of GaN-based LEDs by pinning defects in nanorod array. Nanomaterials. 2022;12(21):3880.
32. Hospodková A, Oswald J, Zíková M, Pangrác J, Kuldová K, Blažek K, et al. On the correlations between the excitonic luminescence efficiency and the QW numbers in multiple InGaN/GaN QW structure. J Appl Phys. 2017;121(21):214505.
33. Kim M, Choi S, Lee JH, Park C, Chung TH, Baek JH, et al. Investigating carrier localization and transfer in InGaN/GaN quantum wells with V-pits using near-field scanning optical microscopy and correlation analysis. Sci Rep. 2017;7:42221.

34. Li P, Li H, Li Z, Kang J, Yi X, Li J, et al. Strong carrier localization effect in carrier dynamics of 585 nm InGaN amber light-emitting diodes. J Appl Phys. 2015;117(7):073101.
35. Marcinkevičius S, Tak T, Chow YC, Wu F, Yapparov R, DenBaars SP, et al. Dynamics of carrier injection through V-defects in long wavelength GaN LEDs. Appl Phys Lett. 2024;124(18):181108.
36. Marcinkevičius S, Ewing J, Yapparov R, Wu F, Nakamura S, Speck JS. Experimental evidence of hole injection through V-defects in long wavelength GaN-based LEDs. Appl Phys Lett. 2023;123(20):201102.
37. Massabuau FCP, Horton MK, Pearce E, Hammersley S, Chen P, Zielinski MS, et al. Optical and structural properties of dislocations in *InGaN*. J Appl Phys. 2019;125(16):165701.
38. Yapparov R, Tak T, Ewing J, Nakamura S, DenBaars SP, Speck JS, et al. Properties of V-defect injectors in long wavelength GaN LEDs studied by near-field electro- and photoluminescence. J Appl Phys. 2024;136(8):083103.
39. Wang H, Ji Z, Qu S, Wang G, Jiang Y, Liu B, et al. Influence of excitation power and temperature on photoluminescence in InGaN/GaN multiple quantum wells. Opt Express. 2012;20(4):3932–40.
40. Chiu YC, Bayram C. Low temperature absolute internal quantum efficiency of InGaN-based light-emitting diodes. Appl Phys Lett. 2023;122(9):091101.
41. Yoo YS, Roh TM, Na JH, Son SJ, Cho YH. Simple analysis method for determining internal quantum efficiency and relative recombination ratios in light emitting diodes. Appl Phys Lett. 2013;102(21):211107.
42. Lu T, Lee TY, Lai S, Dai Y, Wu R, Gong Z, et al. Improving optoelectronic performance and modulation bandwidth of green micro-LEDs via a compound pre-strained strategy. Opt Lett. 2024;49(4):883–6.
43. Iida D, Ohkawa K. Recent progress in red light-emitting diodes by III-nitride materials. Semicond Sci Technol. 2022;37(1):013001.
44. Li Q, Xu SJ, Xie MH, Tong SY. Origin of the 'S-shaped' temperature dependence of luminescent peaks from semiconductors. J Phys Condens Matter. 2005;17(30):4853–8.
45. Zheng X, Zhang K, Lu Z, Zhou M, Huang T, Fu Y, et al. Impact of localization on the optical properties of InGaN-based red light-emitting diodes grown on a silicon substrate. ACS Photon. 2024;11(4):1464–72.
46. Zheng X, Tong C, Liu Y, Ai S, Fu Y, Zhou M, et al. Limited impact of the sidewall effect in dependence of temperature for InGaN-based blue micro-LEDs grown on a silicon substrate. Opt Lett. 2024;49(17):4867–70.
47. Jia C, Shen C, Wang Q. Performance improvement of *InGaN* red light-emitting diode by using V-pits layer and step-graded *GaN* barrier. Phys Status Solidi A. 2023;220(13):2300086.
48. Chow YC, Tak T, Wu F, Ewing J, Nakamura S, DenBaars SP, et al. Origins of the high-energy electroluminescence peaks in long-wavelength (∼495–685 nm) InGaN light-emitting diodes. Appl Phys Lett. 2023;123(9):091103.
49. Park JH, Pristovsek M, Cai W, Cheong H, Kang CM, Lee DS, et al. Dislocation suppresses sidewall-surface recombination of micro-LEDs. Laser Photon Rev. 2023;17(10):2300199.
50. Wang Z, Zhu S, Shan X, Yuan Z, Qian Z, Lu X, et al. Red, green and blue InGaN micro-LEDs for display application: temperature and current density effects. Opt Express. 2022;30(20):36403–13.
51. Rienzi V, Smith J, Lim N, Chang H-M, Chan P, Wong MS, et al. Demonstration of III-nitride red LEDs on Si substrates via strain-relaxed template by InGaN decomposition layer. Crystals. 2022;12(8):1144.
52. Ewing JJ, Lynsky C, Wong MS, Wu F, Chow YC, Shapturenka P, et al. High external quantum efficiency (6.5%) InGaN V-defect LEDs at 600 nm on patterned sapphire substrates. Opt Express. 2023;31(25):41351–60.
53. Chhajed S, Cho J, Schubert EF, Kim JK, Koleske DD, Crawford MH. Temperature-dependent light-output characteristics of GaInN light-emitting diodes with different dislocation densities. Phys Status Solidi A. 2011;208(4):947–50.
54. Schubert EF. Light-emitting diodes. 2nd ed. Cambridge University Press, New York. 2006.
55. Kim MS, Lee HK, Yu JS. Device characteristics and thermal analysis of AlGaInP-based red monolithic light-emitting diode arrays. Semicond Sci Technol. 2013;28(2):025005.
56. Li P, David A, Li H, Zhang H, Lynsky C, Yang Y, et al. High-temperature electroluminescence properties of InGaN red 40 × 40 μm^2 micro-light-emitting diodes with a peak external quantum efficiency of 3.2%. Appl Phys Lett. 2021;119(23):231101.

Publisher's Note

Springer Nature remains neutral with regard to jurisdictional claims in published maps and institutional affiliations.